Available online at www.sciencedirect.com
ScienceDirect
Journal of Nuclear Materials 361 (2007) 160–173
journal of nuclear materials
www.elsevier.com/locate/jnucmat

Role of grain boundary engineering in the SCC behavior of ferritic–martensitic alloy HT-9

G. Gupta [a,*], P. Ampornrat [a], X. Ren [b], K. Sridharan [b], T.R. Allen [b], G.S. Was [a]

[a] University of Michigan, 2940 Cooley, 2355 Bonisteel Blvd, Ann Arbor, MI 48019, USA
[b] University of Wisconsin, Madison, WI 53706, USA

Abstract

This paper focuses on the role of grain boundary engineering (GBE) in stress corrosion cracking (SCC) of ferritic–martensitic (F–M) alloy HT-9 in supercritical water (SCW) at 400 °C and 500 °C. Constant extension rate tensile (CERT) tests were conducted on HT-9 in as-received (AR) and coincident site lattice enhanced (CSLE) condition. Both unirradiated and irradiated specimens (irradiated with 2 MeV protons at 400 °C and 500 °C to a dose of 7 dpa) were tested. Ferritic–martensitic steel HT-9 exhibited intergranular stress corrosion cracking when subjected to CERT tests in an environment of supercritical water at 400 °C and 500 °C and also in an inert environment of argon at 500 °C. CSL-enhancement reduces grain boundary carbide coarsening and cracking susceptibility in both the unirradiated and irradiated condition. Irradiation enhanced coarsening of grain boundary carbides and cracking susceptibility of HT-9 for both the AR and CSLE conditions. Intergranular (IG) cracking of HT-9 results likely from fracture of IG carbides and seems consistent with the mechanism that coarser carbides worsen cracking susceptibility. Oxidation in combination with wedging stresses is the likely cause of the observed environmental enhancement of high temperature IG cracking in HT-9.

1. Introduction

One of the most promising advanced reactor concepts for Generation IV nuclear reactors is the supercritical water reactor (SCWR). Operating above the thermodynamic critical point of water (374 °C, 22.1 MPa), the SCWR offers many advantages compared to current LWRs including the use of a single phase coolant with high enthalpy, the elimination of components such as steam generators, steam separators, dryers, and a low coolant mass inventory resulting in smaller components, and a much higher efficiency. Since SCW has never been used in nuclear power applications, there are numerous potential problems, particularly with materials. Depending upon the species present and the oxygen content in the solution, SCW can become a very aggressive oxidizing environment. This is a cause of concern in regards to both general corrosion and stress corrosion cracking (SCC) of the structural materials and fuel elements of the reactors.

Ferritic–martensitic (F–M) alloy HT-9 has been identified as a candidate core structural alloy in SCWR. Preliminary studies have shown that HT-9 experiences high corrosion rates in the SCWR [1].

* Corresponding author. Tel./fax: +1 734 936 0266.
E-mail address: gauravg@umich.edu (G. Gupta).

0022-3115/$ - see front matter © 2006 Elsevier B.V. All rights reserved.
doi:10.1016/j.jnucmat.2006.12.006

HT-9 also exhibits IGSCC in SCW at 400 °C and 500 °C [1,2]. Initial studies have shown that proton irradiation at 400 °C and 500 °C enhances cracking in SCW [2]. Irradiation enhances diffusion and/or precipitate redistribution, which can enhance recovery and coarsening.

Grain boundary engineering (GBE) is being explored as a means of reducing the susceptibility of HT-9 to IGSCC in SCW. GBE involves a series of thermo-mechanical treatments designed to change the grain boundary structure by increasing the low angle boundary or coincident site lattice boundary (CSLB) fraction. Due to an increased structural order and reduced free volume, these boundaries exhibit relatively low energy and less segregation, thus providing resistance to intergranular corrosion. Another potential benefit of GBE is that these special boundaries induce slip in neighboring grains by either transmitting or absorbing and re-emitting lattice dislocations, thereby reducing grain boundary stresses and propensity for crack formation [3].

According to work done by Hertzberg et al. [4] fracture in steels is generally initiated at the inclusions or precipitate particles. The critical stress to propagate a crack is inversely proportional to the length the crack [4]. If it is assumed that the crack length at initiation is equal to the diameter of the carbide particle then the fracture stress will decrease with increasing precipitate size. Irradiation leads to coarsening of the precipitates (including carbides) in addition to the coarsening which occurs under load and temperature. Lechtenberg et al. [5] observed that embrittlement of HT-9 is associated with increased grain boundary carbide precipitation and coarsening. Gelles et al. [6] and Kai et al. [7] attributed a decrease in fracture stress and an increase in DBTT to particle coarsening during irradiation. It is believed that coarsening of these particles would be less in grain boundary engineered specimens as these low misorientation boundaries have a lower diffusivity that should result in slower coarsening rate. Thus if cracking in HT-9 is initiated at carbide particles, GBE should reduce susceptibility to SCC.

Kim et al. [8], Palumbo et al. [9], Lehockey et al. [10] and Alexandreanu et al. [11] have demonstrated the beneficial influence of GBE in mitigating SCC in austenitic alloys and Ni-base alloys. Little work has been reported on F–M alloys. Gupta et al. [12,13] have demonstrated the beneficial influence of GBE on creep properties of F–M alloy T91. It is envisaged that CSL-enhancement would improve the SCC behavior of F–M alloy HT-9 in SCW both with and without the effect of irradiation due to the reasons discussed above.

The purpose of the current study is to investigate the effect of GBE on SCC of F–M alloy HT-9 for use as structural material in the SCWR. CERT tests were conducted in deaerated water at 400 °C and 500 °C on unirradiated and irradiated F–M alloy HT-9 in the as-received (AR) and CSL-enhanced (CSLE) condition to observe the effect of GBE on the susceptibility of HT-9 in SCW. Further, microstructural characterization was performed on the specimens in the AR and CSLE condition both before and after the CERT test to understand the role of GBE on the SCC behavior of HT-9.

Because the dissolved oxygen concentration has been shown to affect the growth of the oxide layer, experiments were also conducted on samples implanted with oxygen to modify the oxide growth during exposure to SCW [14]. These studies showed a smaller weight gain for the surface modified (SM) HT-9 during exposure experiments at 500 °C in SCW as compared to unmodified HT-9. It was envisaged that surface modification might also improve the SCC resistance of HT-9 in SCW. Therefore, SCC experiments were conducted on SM HT-9 in SCW at 500 °C in both the irradiated and unirradiated condition.

2. Experiment

2.1. Material and sample fabrication

The chemical composition of HT-9 heat used in this study is given in Table 1. Samples in the form of tensile bars with a gage length of 21 mm and a cross-section of 2 mm × 2 mm were fabricated via

Table 1
Chemical composition of HT-9 (in wt%) used in this study

Alloy	Cr	Mo	Mn	V	Ni	Si	Cu	C	P	Al	S	N	Fe
HT-9[a]	11.63	1.00	0.52	0.30	0.50	0.22	0.04	0.20	0.02	0.01	0.006	0.047	Bal.

[a] Normalization: 0.5 h at 1040 °C (air cooled), tempered: 1 h at 760 °C (air cooled).

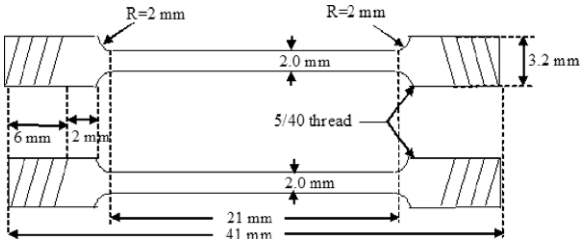

Fig. 1. Dimensions of tensile bars used for CERT experiments in SCW.

electric discharge machining, Fig. 1. The standard heat treatment consisted of a solution anneal at 1040 °C for 30 min to completely austenitize the microstructure and dissolve the carbides, followed by air-cooling and then tempering at 760 °C for 60 min to relieve the stresses and enhance toughness (Note that this heat-treatment was given to the alloy plate prior to sample fabrication via EDM.). This heat-treatment resulted in large grains of approximately 50 μm. Further, all the tensile bars were mechanically polished by SiC abrasive paper up to a grit of 4000 and then electropolished in a solution of 10% perchloric acid and 90% methanol at −30 °C and 40 V before being used for CERT tests (This ensured the removal of the remelt layer from EDM process, as the thickness of the remelt layer is ~5 μm on each side, while ~70 μm were removed by polishing on each side.).

2.2. Microstructural characterization of HT-9

HT-9 is a low carbon steel that is used in the two phase, ferritic–martensitic structure. The microstructure consists of tempered martensite laths forming subgrains in a ferrite matrix, with carbides and (V, Nb) carbonitrides precipitated mainly on dislocations within the subgrains and on the prior austenite grain boundaries (PAGBs). The subgrain structure produced by martensitic transformation and the precipitation of carbides and carbonitrides are the primary microstructural features responsible for high temperature strength. Fig. 2 shows the microscopic images of HT-9 depicting various

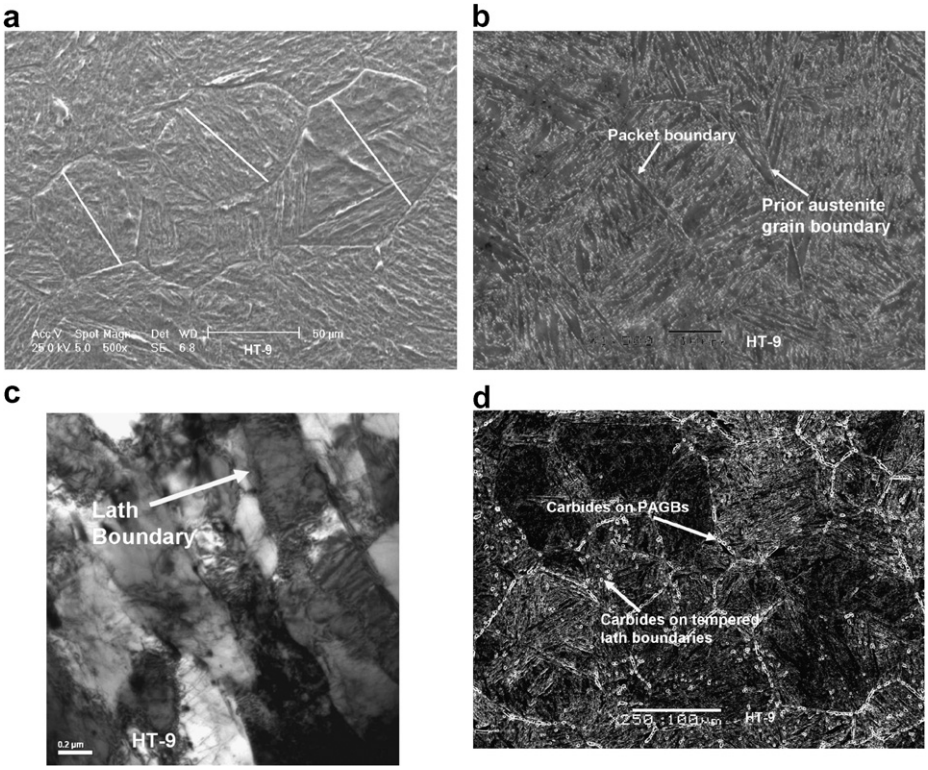

Fig. 2. Microstructure of HT-9; (a) SEM image showing the average grain size, (b) SEM image of a grain depicting the prior austenite grain boundary and packet boundary, (c) SEM image showing the carbides on the prior austenite grain boundaries and lath boundaries and (d) TEM image of lath structure in HT-9.

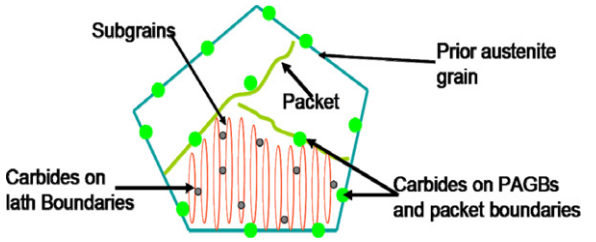

Fig. 3. Microstructure of HT-9 in the as-received condition (a) SEM image, and (b) Schematic.

microstructural features; Fig. 2(a) is a SEM image which shows the average grain size of 50 μm, Fig. 2(b) is a magnified SEM image to show the prior austenite grain boundary and packet boundaries in HT-9, Fig. 2(c) is a TEM image showing the typical lath structure and Fig. 2(d) is a SEM image of the carbides on the PAGB and lath boundaries.

In performing grain boundary engineering on HT-9, it is vital to fully understand the microstructure so as not to alter key elements of the microstructure by the GBE process. In order to get a simplified and clearer image of this complex microstructure it is easy to understand it with a schematic. Fig. 3 shows a schematic illustration of the microstructure of HT-9 after tempering. The regions within a grain with the same habit plane and orientation define a packet which is the smallest microstructural unit of martensite. The packet boundaries and the PAGBs are generally the high-angle boundaries. During tempering carbides and carbonitrides precipitate on the PAGBs and lath boundaries. The diffusion rate along high-angle boundaries such as random boundaries is higher than that along low-angle boundaries. Carbides are expected to be formed more easily on the PAGBs because these boundaries act as the faster diffusion paths. Dislocations rearrange to form subgrains within the laths (a subgrain is basically a sub-structure within the deforming grain, bounded by dislocation networks and formed due to misorientations).

2.3. Grain boundary engineering

Earlier work done by Gupta et al. [15] on grain boundary engineering of F–M alloy T91 has shown that the fraction of low angle boundaries (Σ1) can be increased by a thermo-mechanical process involving 5% strain + 1040 °C: 1 h + 800 °C: 0.66 h, air cool without changing the other microstructural features such as grain size and carbide size, location, and number density. Due to the similarity of microstructural features in T91 and HT-9 a similar thermo-mechanical treatment of HT-9 involving 5% strain + 1040 °C: 0.5 h + 760 °C: 1 h, air cool was performed successfully to increase the fraction of low angle boundaries (Σ1). The prior austenite grain sizes were similar in the two conditions (AR and CSLE). In order to measure the fraction of these special boundaries, in HT-9 Orientation Imaging Microscopy (OIM) was used. Typically OIM scans were performed over an 80 μm × 60 μm area with a step size of 0.1 μm. For OIM analysis samples were carefully prepared metallographically by grinding with SiC abrasive paper up to 4000 grit followed by polishing with colloidal silica solution.

Due to the complex nature of the microstructure it is important to determine which boundaries are actually modified by CSL-enhancement. OIM analysis shows an increase in the fraction of Σ1 boundaries from the AR condition to the CSLE condition. These low angle boundaries include the subgrain boundaries as well as tempered lath boundaries. Theoretically, a Σ1 boundary denotes a perfect (or nearly perfect) crystal; i.e. no boundary. However boundaries relatively close to the Σ1 orientation are those with only small misorientations (greater than 0° but less than 15°) called 'small-angle grain boundaries' – and they are subsumed under the term Σ1 boundaries. The fraction of these low angle boundaries with misorientation less than 3° is higher in CSLE samples as compared to AR samples by about 30% (Fig. 4). These are typically the subgrain boundaries.

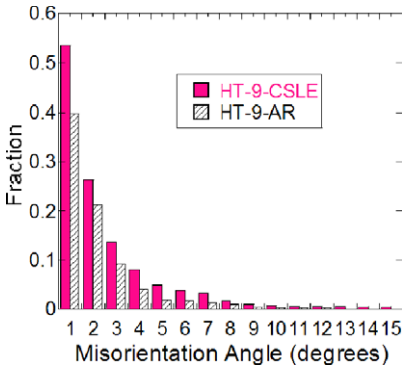

Fig. 4. Plots of Σ1 boundary in AR and CSL-enhanced conditions in F–M alloy HT-9.

2.4. Surface modification

HT-9 SCC bars were ion implanted with oxygen at about 40 kV to a dose of 3×10^{17} ions/cm^2, using the plasma immersion ion implantation (PIII) process [16]. Fig. 5(a) and (b) shows the arrangement of the SCC samples on the PIII stage and a schematic illustration of the PIII process, respectively. All the SCC samples were placed on rectangular Al strips in a manner that the gage length made complete contact with the Al strip and the threaded ends hung out. This ensured that gage length part received sufficient cooling and did not get heated due to the energy of the implanting ions. The depth of the modified region was approximately 0.15 μm (Note here that EDM-ed surfaces on SCC specimens were mechanically polished by grinding on a SiC abrasive paper up to 4000 grit and then electropolished to remove the remelt layer prior to surface implantation).

2.5. Proton irradiation

F–M alloy HT-9 in the AR, CSLE, and SM conditions was irradiated with 2 MeV protons at 400 ± 10 °C and 500 ± 10 °C to a dose of 7 dpa at a dose rate of 2×10^{-5} dpa/s. Proton irradiations were performed on tensile bars using a specially designed stage connected to the General Ionex Tandetron accelerator at the Michigan Ion Beam Laboratory. The experimental details can be found elsewhere [17].

2.6. Stress corrosion cracking experiments

Constant extension rate tensile (CERT) tests were performed in the multi-sample supercritical water system. Table 2 gives a summary of the CERT tests conducted on HT-9 samples in various conditions (Note here that one sample was tested for each condition.). The tensile samples were strained at a rate of 3×10^{-7} s^{-1}. During exposure, the temperature inside the autoclave was controlled to within ± 5 °C of the target temperature. The pressure was maintained at 25.2 ± 0.1 MPa. High purity water was used as test medium and the dissolved oxygen (DO) content was maintained below 10 ppb at inlet and outlet by purging argon gas continuously. Both inlet and outlet conductivities were less than 0.1 μS/cm. The flow rate was maintained at about 65 ml/min.

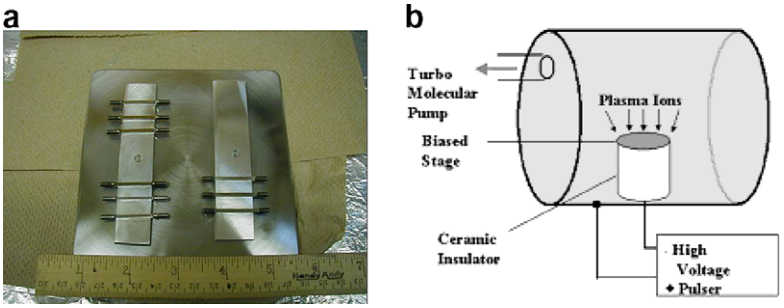

Fig. 5. (a) Arrangement of samples for surface modification and, (b) schematic illustration of the plasma immersion ion implantation (PIII) system.

Table 2
Summary of the CERT tests conducted on HT-9

Temp (°C)		Alloy condition	Environment
Irrad.	CERT		
–	400	HT-9 AR	Deaerated SCW
–	500	HT-9-SM, HT-9 AR, HT-9 CSLE	Deaerated SCW
500	400	HT-9 AR(7 dpa)	Deaerated SCW
400	400	HT-9 AR(7 dpa)	Deaerated SCW
500	500	HT-9 CSLE, HT-9 AR, HT-9-SM (both at 7 dpa)	Deaerated SCW
500	500	HT-9 AR(7 dpa)	Argon
–	500	HT-9 AR	Argon

AR = As received, SM = surface modified, CSLE = grain boundary engineered.

Since earlier CERT experiments provided evidence of intergranular (IG) cracking in HT-9 [1,3] further CERT tests were conducted where both unirradiated and irradiated HT-9 samples were tested at 500 °C in both SCW and argon in order to isolate the effect of microstructure, irradiation and environment on the cracking behavior of HT-9. Further to understand the role of surface modification, independent experiments were performed by exposing HT-9 steel in the as-received and oxygen ion implanted conditions to SCW at 500 °C.

2.7. Fractography

Following CERT tests, the samples were examined using a Philips XL-30 scanning electron microscope (SEM). The fracture surface and the faces of the sample gage sections were analyzed. Crack analysis was performed on cross-section of SCC samples prepared by mounting in epoxy resin followed by mechanical polishing. The mounted specimens were etched in a solution of 1 part HCl to 3 parts HNO_3 in order to observe the grain boundaries. The cracks were investigated in SEM in both secondary-electron (SE) and back scattered-electron modes. The crack depth was measured from the deepest part of crack to the outer oxide layer. Analysis of cracks on HT-9 was performed on three areas of SCC bars; marked as A, B and C, Fig. 6. These areas are defined by the width in the necked region to that in the un-necked region. Area A is from gage fracture to 80% of original width, area B is from 80% to 90%, and area C is from 90% to un-necked width. Area A is characterized by extensive localized plastic deformation and no crack analysis was performed in this region. Cracks were recorded only in areas B and C.

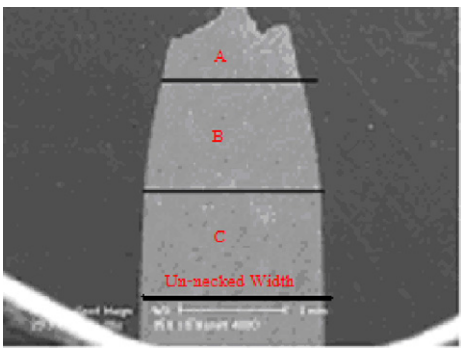

Fig. 6. Low magnification image of fractured SCC sample of HT-9.

3. Results

3.1. Irradiated microstructure

Carbide coarsening during irradiation at 500 °C was measured at PAGBs. The carbide size at PAGBs in the AR condition increased from 365 ± 15 nm to 405 ± 17 nm after irradiation (Fig. 7). Error bars depict the standard deviation from a set of 30 readings. Minimal or no coarsening was observed for carbides on the lath boundaries.

3.2. Surface modified corrosion samples

The SM samples used in exposure tests were characterized for weight gain and the structure and morphology of the oxide layer itself were characterized by scanning electron microscopy (SEM), X-ray diffraction, and electron backscattered imaging techniques [18]. It was observed that the weight gain of the SM samples was higher for lower exposure durations, but for longer durations the weight gain was higher for the untreated samples (Fig. 8).

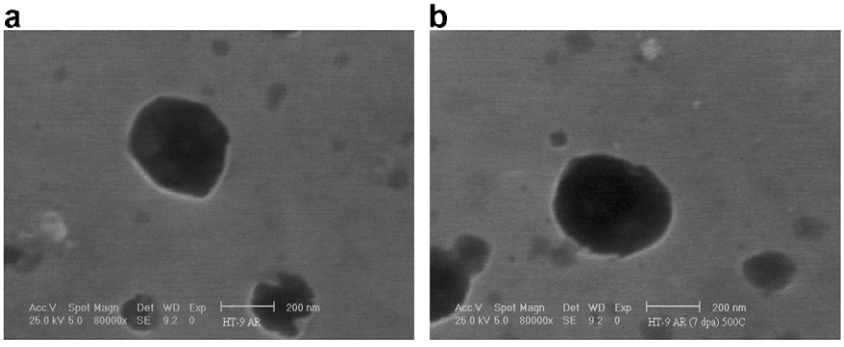

Fig. 7. SEM image of the carbide particles on PAGB in the (a) AR condition and, (b) AR condition after irradiation at 500 °C to 7 dpa.

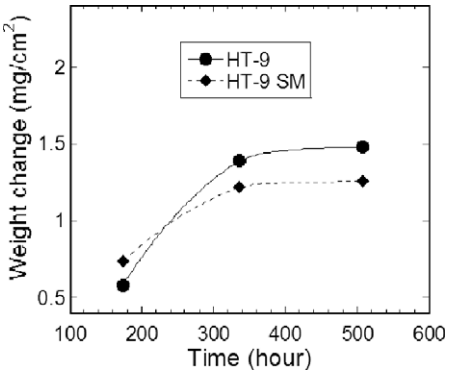

Fig. 8. Plot of weight gain for untreated and SM HT9 in SCW at 500 °C.

Fig. 9 shows results of the XRD analysis for both the AR and SM specimens after exposure time of 1, 2 and 3 weeks in SCW at 500 °C. The standard pattern for magnetite is indicated in the figures by vertical dashed lines. The XRD relative peak intensities of AR samples with various exposure periods were very similar and close to those of standard magnetite. However, for SM samples, only the samples exposed for 505 h showed these relative peak intensities, whereas some preferred crystal orientations (texture) appeared in samples exposed to shorter exposure time (172 and 333 h). The preferred orientations are (1 1 1) and (1 1 0) for 172 and 333 h exposed samples, respectively.

3.3. CERT experiments

Table 3 gives a summary of the results obtained in the CERT tests on HT-9. With an increase in test temperature the yield stress and maximum stress decrease while elongation increases. Irradiations lead to an increase in the yield stress and maximum stress along with a decrease in percent elongation and reduction in area. Samples irradiated at the lower temperature had higher yield stress and maximum stress and lower values of percent elongation compared to the samples irradiated at higher temperature. CSLE specimens had a higher percent elongation and higher reduction in area and similar values of stresses when compared with AR specimens under similar test conditions for both the irradiated and unirradiated conditions. Note that the irradiated specimens are basically composite samples with 25 μm of irradiated region (only one side of the tensile bars is irradiated during proton irradiations [17]) and the balance being unirradiated. The strains to failure for all the unirradiated and irradiated HT-9 were very similar. However, the CSLE samples exhibited a small but consistent increase in strain to failure as compared to the AR condition as shown in Fig. 10 for both unirradiated and irradiated samples. Surface modification does not affect the mechanical properties (yield stress, maximum stress, % elongation and reduction in area) in either the unirradiated or irradiated conditions. Note here

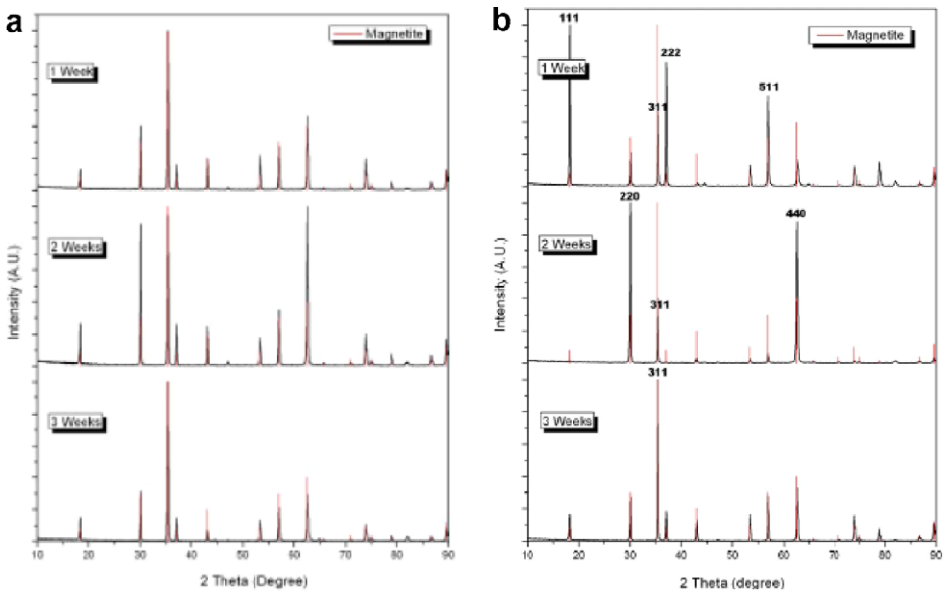

Fig. 9. XRD plots showing analysis of the oxide layers for the (a) untreated and, (b) SM specimen of HT-9 after exposure tests in SCW at 500 °C.

Table 3
Results of CERT tests conducted on HT-9

Temp (°C)		Alloy condition	Environment	Yield stress (MPa)	Max stress (MPa)	RA%	Elong %
Irrad.	CERT						
–	400	HT-9 AR	Deaerated SCW	490	575	51.5	12.1
–	500	HT9 AR	Deaerated SCW	471	482	63.6	14.4
500	400	HT-9 AR(7 dpa)	Deaerated SCW	495	590	50.1	11.0
400	400	HT-9 AR(7 dpa)	Deaerated SCW	520	640	34.3	10.1
500	500	HT-9 AR(7 dpa)	Deaerated SCW	474	484	62.9	14.4
–	500	HT-9 AR	Deaerated SCW	463	478	63.4	14.7
500	500	HT-9 AR(7 dpa)	Argon	477	491	63.6	14.8
–	500	HT-9 AR	Argon	469	482	64.1	14.9
500	500	HT-9 CSLE (7 dpa)	Deaerated SCW	473	486	65.2	14.8
–	500	HT-9 CSLE	Deaerated SCW	461	473	68.5	15.3
500	500	HT-9 SM	Deaerated SCW	471	480	63.1	14.4
–	500	HT-9 SM	Deaerated SCW	462	477	63.5	14.8

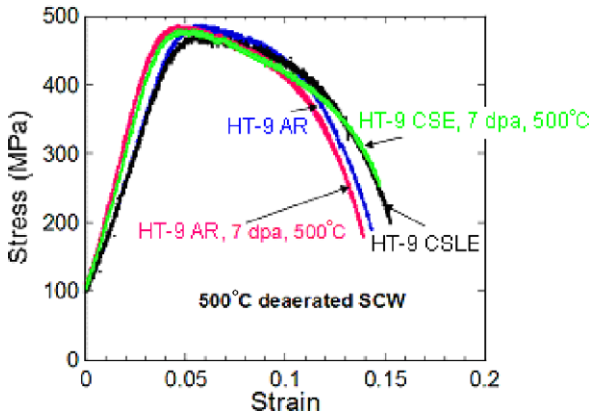

Fig. 10. Plot of stress vs. strain for CERT test in deaerated SCW at 500 °C for HT-9 AR and HT-9 CSLE samples in both the unirradiated and irradiated (at 500 °C to 7 dpa) conditions.

that the limited number of experiments may preclude a strict quantitative analysis and comparison, the general trend is more important.

Microstructural characterization was performed on AR and CSLE specimens in gage sections both before and after CERT test at 500 °C. Carbide size on the PAGB was measured for both the AR and CSLE specimen after the CERT test and compared to its size before the CERT test. The carbide size on PAGBs in both the AR and CSLE conditions before the CERT test was similar. It was observed that CSL-enhancement led to reduced coarsening of the carbides on PAGBs. Fig. 11(a) and (b) shows the carbide size on PAGBs for both the AR and CSLE conditions. The carbide size increased from 363 ± 16 nm to 410 ± 20 nm in the CSLE condition and from 365 ± 15 nm to 455 ± 21 nm in the AR condition. The error bars were obtained as standard deviation from a data set of 30 readings.

3.4. Fractography

Examination of the side surface of the sample provided evidence of cracking in HT-9. Cross-section

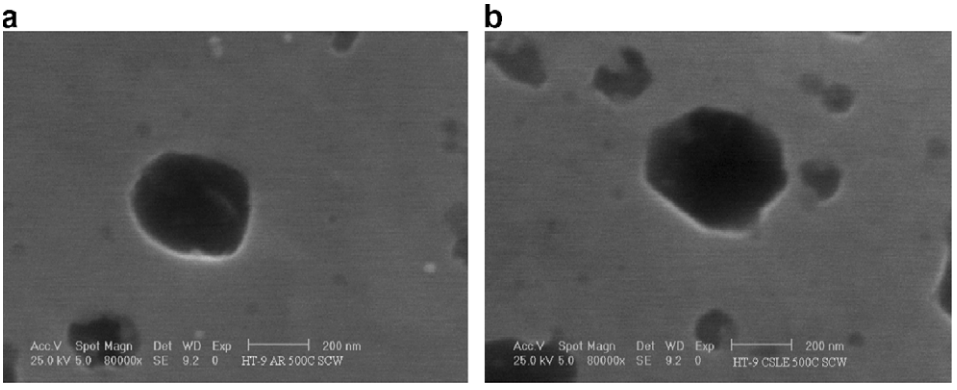

Fig. 11. SEM image of carbide at the PAGB after CERT test in SCW at 500 °C in the (a) AR and, (b) CSLE condition.

Table 4
Summary of the results of cracking analysis on HT9 for CERT tests

Alloy	Environment	Temp(°C)		Max crack length (μm)	Crack density (#/mm^2)
		CERT	Irrad.		
HT-9 AR	SCW	400	–	3.80	5.0
HT-9 AR	SCW	500	–	13.2	22.5
HT-9 AR	SCW	400	500	6.20	8.75
HT-9 AR	SCW	400	400	12.6	13.75
HT-9 AR	SCW	500	500	18.4	28.75
HT-9 AR	Argon	500	–	8.30	2.50
HT-9 AR	Argon	500	500	9.10	3.75
HT-9-CSLE	SCW	500	–	10.2	15.0
HT-9-CSLE	SCW	500	500	13.2	17.5
HT-9-SM	SCW	500	–	11.5	21.0
HT-9-SM	SCW	500	500	17.5	27.0

analysis was done according to the process described earlier. IG cracking was evident in HT-9 under all the test conditions. Table 4 gives a summary of the crack analysis done for HT-9 under all test conditions. Cracking susceptibility increases with temperature, oxygen content and irradiation with cracking being more severe at lower irradiation temperature. Cracking has been reported in terms of crack density and also maximum crack depth.

Fig. 12 shows a plot of maximum crack depth and crack density for HT-9, HT-9-SM and HT-9-CSLE for CERT tests at 500 °C in SCW for both the unirradiated and irradiated conditions. CSLE samples had lower cracking as compared to the AR samples under similar test conditions in both the irradiated and unirradiated case. Similarly the SM samples had lower cracking than the AR samples in both the unirradiated and irradiated conditions though the difference is insignificant in irradiated samples. In terms of cracking the irradiated CSLE sample behaved similar to the AR unirradiated condition (the maximum crack depth was similar in the two conditions, while the crack density was lower in the irradiated CSLE condition). Essentially, CSL-enhancement mitigates the effect of irradiation on cracking. Fig. 13 displays IG cracking in HT-9 and HT-9-CSLE tested at 500 °C in deaerated SCW for four test conditions; (a) AR, (b) AR-Irradiated (500 °C, 7 dpa), (c) CSLE and (d) CSLE-Irradiated (500 °C, 7 dpa).

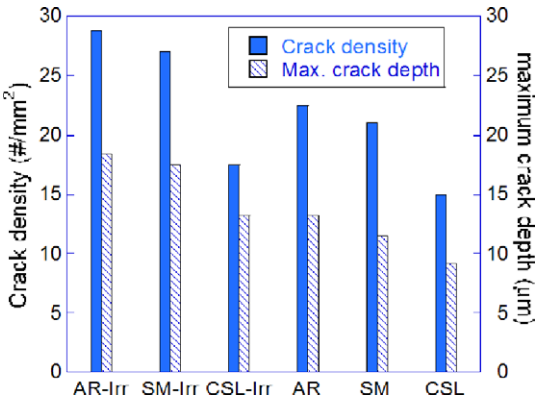

Fig. 12. Plot of maximum crack depth and crack density for HT-9 for all unirradiated specimens and irradiated conditions.

4. Discussion

4.1. Intergranular fracture in HT-9

In this study, IG cracking in HT-9 was observed in an inert environment of argon, suggesting that the microstructure of HT-9 plays a role in the inherent susceptibility to IG cracking. Alamo et al. [19] observed intergranular fracture in addition to some ductile regions with dimples in HT-9 irradiated to a dose of 3.4 dpa at 325 °C in the Osiris reactor and tested at 20 °C in air. It is well established that ductile failure is initiated by the nucleation of voids at second phase particles. There is evidence in the literature that fracture in steels is generally initiated at second phase particles or inclusions [4,20–23]. The voids form either by cracking of the particles, or by decohesion at the particle/matrix interfaces [24,25]. The strain required for void nucleation decreases with increasing volume fraction of carbides, which in turn can be linked to the carbon content of the steel. The formation of voids begins as a result of high stresses imposed by dislocation arrays on individual hard particles. The coarser particles lead to higher local stress concentrations, which

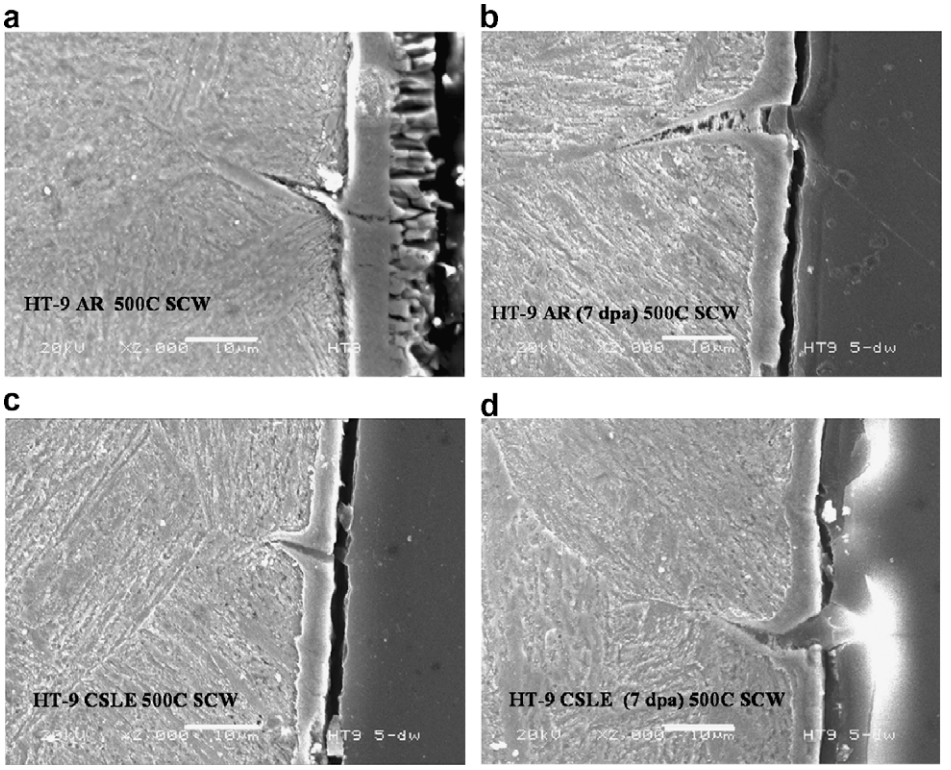

Fig. 13. SEM images showing IG cracks in HT-9 fractured specimens after CERT tests in deaerated SCW at 500 °C for the following conditions; (a) AR, (b) AR-irradiated at 500 °C to 7 dpa, (c) CSLE and (d) CSLE-irradiated at 500 °C to 7 dpa.

cause localized rupture and microcrack formation [4].

HT-9 steel contains twice as much carbon as does T91 and HCM12A steel. In the normalized-and-tempered condition, it contains almost twice as much precipitates (3.8 wt% precipitates in HT-9 as compared to 1.5 wt% in T91) [26]. Measurements made in this study show a linear carbide density of 2.2 μm^{-1} in HT-9 AR (Fig. 14) as compared to 1.5 μm^{-1} in T91 AR on PAGBs [15], confirming the greater volume fraction of carbide in HT-9 vs. T91. Thus the high level of carbon results in greater carbide volume fraction and coarser grain boundary carbides.

There are other microstructural features that might be contributing factors, although they have not been explored as yet. The absence of niobium in HT-9 leads to a large initial prior austenite grain size [27]. For quenched and tempered steels, a small prior austenite grain size improves SCC resistance [28] due to the lower back stresses as expected from Hall–Petch relationship [21]. The grain size of HT-9 used in this study is almost four times that of T91 and HCM12A, neither of which exhibited cracking.

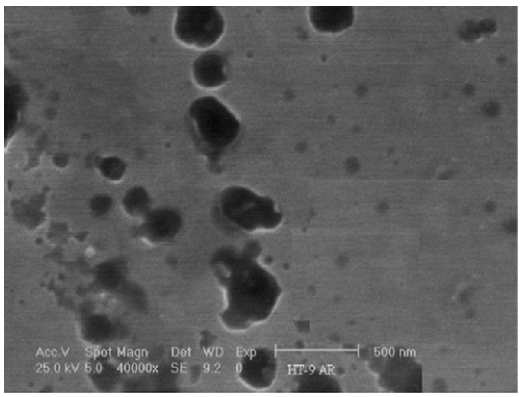

Fig. 14. SEM image of HT-9 AR showing the linear carbide density on PAGB.

A large austenite grain size, under the same test conditions, should increase the embrittlement because the size of the dislocation arrays impinging on the grain boundary carbides will be larger and thus more effective in forming crack nuclei. Another factor is the presence of δ-ferrite in HT-9 (absent in T91 and HCM12A), which can be a major cause of decrease in strength. Work by Schafer et al. [29]

indicates that fracture is initiated at carbide particles on the δ-ferrite/martensite interface.

From the available data in literature and this study on fracture of HT-9, IG cracking likely results from fracture of grain boundary carbides. Higher carbon content and coarser carbides cause greater amounts of IG cracking. The following sections will review the dependencies of IG fracture on grain boundary character, irradiation and the environment in light of the role of grain boundary carbides.

4.2. Role of GBE in intergranular fracture of HT-9

The effect of GBE on HT-9 in SCW can be understood by comparing the tensile behavior of the AR and CSLE conditions for HT-9 under similar test conditions. In both the unirradiated and irradiated conditions the CSLE samples displayed a higher strain to failure as compared to AR samples. Similar observation was made in the case of T91 where the CSLE condition displayed higher strain to failure and a larger reduction in area for both irradiated and unirradiated condition [2].

The CSLE specimens exhibited less cracking as compared to the AR specimen for both unirradiated and irradiated conditions. Due to the lower diffusivity of these special CSL or low angle boundaries the coarsening of the precipitates should be reduced. This suggestion was confirmed by measurement in which coarsening of grain boundary carbides in the AR sample was double that of the CSLE sample. Studies done by Singhal et al. [30] and by Lim et al. [31] have shown that coarse precipitates were observed more on high-angle boundaries and that it is related to the energy of the boundary. Gunther et al. [32] in his study on the carbide density and grain boundary character in tempered martensitic steel HT-9 has shown that carbides grow and precipitate more easily when grain boundary energies and diffusivities are higher. They suggested in their results that certain micrograin boundaries are more suitable to nucleation and growth of carbides as compared to the others. If carbides do indeed act as sites for crack initiation, then coarser carbides are more prone to fracture. Since CSL-enhancement leads to reduced coarsening, then the beneficial effect of the CSLE process is the suppression of coarsening of the grain boundary carbides.

4.3. Role of environment

The susceptibility to cracking of HT-9 increased in going from an argon environment to the deaerated water to the 300 ppb oxygen containing water at the same temperature. Steven et al. [33] observed evidence of IG cracking in HT-9 in CERT tests in oxygenated water at 100–230 °C and they related this to higher strength and lower toughness of HT-9 and the presence of precipitates at prior austenite grain boundaries. This increase in cracking with more aggressive environment can be explained if it is assumed that cracking is initiated due to the formation of microcracks at grain boundary carbide particles. The process of microvoid coalescence can be modified by the influence of the environment during the subsequent plastic flow and breakage of the ligaments between the voids. Oxidation occurs rapidly in F–M alloys in high temperature SCW, where the fresh metal exposed by crack nuclei oxidizes and ruptures [34]. The rapid growth of oxides may create wedging stresses in the cracks which promotes additional crack growth. Fig. 15 shows

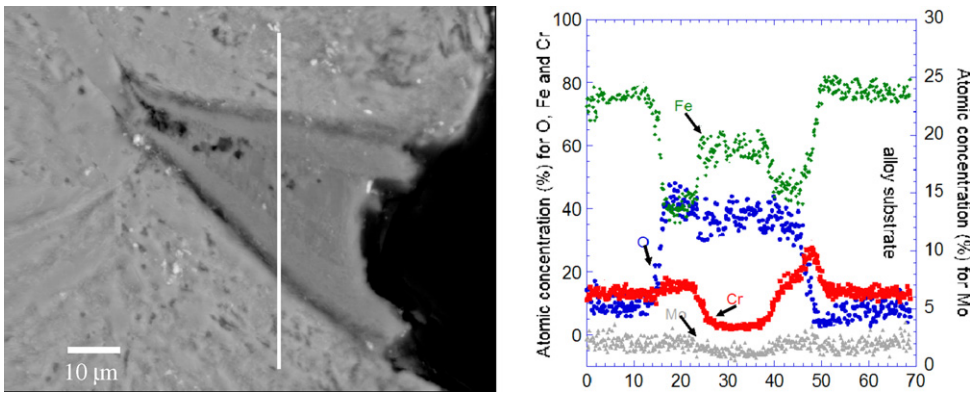

Fig. 15. Intergranular crack on HT-9 tested at 500 °C deaerated SCW and the EDS line scan across the crack.

the EDS scan inside a crack for HT-9 tested in SCW at 500 °C. Two distinct oxide layers were observed, a Cr-rich iron oxide in contact with the metal and an iron oxide in the middle. This is similar to what has been observed on the surface by Pantip et al. [1], indicating that the oxide morphology and perhaps the oxide growth rate in a crack is similar to that observed on the surface. The micrograph clearly demonstrates that the oxide (which has a higher specific volume that the base metal from which it forms) will exert pressure at the crack tip and make it grow. Oxide growth in the crack is occurring nearly perpendicular to the direction of crack propagation. From corrosion experiments conducted by Pantip et al. [1] on HT-9 at 500 °C in SCW the growth rate of the oxide film was observed to be approximately 1.17 μm/h. This is higher than the average crack growth rate (CGR) for HT-9 at 500 °C in SCW (0.068 μm/h), providing support for the idea that the CGR could be influenced by oxide growth.

That IG cracking was observed in HT-9 not only in SCW but also in an inert environment of argon suggests that an aggressive environment is not responsible for the inherent susceptibility to cracking but plays an important role in enhancing crack growth. Further, since T91 and HCM12A, two F–M alloys with similar composition to HT-9, do not crack in the most aggressive environment emphasizes the fact that environment alone is not responsible for cracking. Rather a combination of environment and microstructure is a determining factor for cracking in HT-9. Oxidation in combination with wedging stresses are the likely cause of the observed environmental enhancement of high temperature IG cracking in HT-9.

4.4. Role of proton irradiation on fracture

The precipitate particles coarsen during irradiation at 400 °C and 500 °C [35], thus causing a decrease in fracture stress and an increase in DBTT, even in the absence of further hardening. At 500 °C, the grain boundary carbides in this study coarsened by 10%, yielding roughly a 33% increase in volume. Even though there is no significant hardening due to irradiation at 500 °C the ΔDBTT does not go to zero due to the coarsening of the large precipitates during irradiation [36]. The larger irradiation-induced shift in DBTT in HT-9 steel compared to T91 steel after irradiation at >300 °C has been attributed to the larger amount of carbide in HT-9 steel and to the irradiation-enhanced coarsening of these precipitates, under the assumption that the precipitates act as crack initiators [27]. Since irradiation enhances coarsening of precipitates, and as discussed earlier, coarser precipitates are more prone to cracking, then it follows that irradiation enhances cracking susceptibility due to the coarsening of the carbides at PAGBs.

4.5. Role of surface modification

It was observed that the weight gain of the SM samples was higher for lower exposure durations, but for longer durations the weight gain was higher for the untreated samples. SEM examination indicated that the oxide was denser (particulate density) for the oxygen ion implanted samples for the lower exposure times. This appears to indicate that the oxygen ion implantation, which results in a high density of nanometer size scale particles in the near surface regions, may have resulted in more nucleation sites in the early stages of oxidation making it more impervious at later stages of growth. The formation of nanometer-sized oxide precipitate particles has been documented in earlier studies on T91 steel [37]. In addition, X-ray diffraction of the samples after exposure indicated a pronounced difference in the texture of the oxide in the early stages of oxide growth. Thus both the oxide growth direction and its physical morphology are influenced by the prior oxygen ion implantation. Further, it is well known that ion implantation induces compressive stresses in the near-surface regions of the material, which may delay the nucleation of cracks. Further evaluation of crack initiation and growth must be performed to provide a better understanding of the role of oxygen ion implantation on the SCC cracking response observed in this study, and this is presently underway. It is likely that any effect of the pre-formed oxide is limited to the crack nucleation stage in CERT tests since the depth of surface modification is only 0.15 μm which is well below the proton irradiation depth of about 25 μm. Thus, after irradiation the difference between the untreated and oxygen ion implanted samples is substantially minimized.

5. Conclusions

- Ferritic–martensitic steel HT-9 exhibited intergranular stress corrosion cracking when subjected to constant extension rate tensile tests in an environment of supercritical water at 400 °C and 500 °C.

- HT-9 exhibited cracking in an inert environment of argon, emphasizing the role of microstructure in the inherent susceptibility to cracking.
- CSL-enhancement reduces cracking susceptibility of HT-9 in both the irradiated and unirradiated condition in SCW.
- Carbide coarsening was reduced in the CSLE condition after CERT test in SCW.
- Irradiation resulted in increased susceptibility to IG cracking.
- Irradiation-induced coarsening of the intergranular carbides in HT-9.
- Intergranular cracking of HT-9 likely results from fracture of intergranular carbides. Further the reduction of cracking in CSLE condition and enhanced cracking observed in irradiated samples seems to be consistent with the mechanism that coarser carbides cause greater amount of cracking.
- A high crack tip oxidation rate in combination with wedging stresses is the likely cause of the observed environmental enhancement of high temperature intergranular cracking in HT-9.
- Surface-modification by oxygen ion implantation reduced cracking susceptibility of HT-9 in both the unirradiated and irradiated conditions; however, the change is insignificant in the irradiated condition.

Acknowledgements

Support for this work was provided by the United States Department of Energy under the NERI (Grant # 3 F-00202) and the I-NERI project (Grant # 3 F-01041). The authors gratefully acknowledge the facilities provided by the Electron Microbeam Analysis Laboratory and Michigan Ion Beam Laboratory at the University of Michigan. The authors would also like to thank Ovidiu Toader and Victor Rotberg of the Michigan Ion Beam Laboratory for their invaluable support in conducting the irradiations.

References

[1] P. Ampornrat, C.B. Bahn, G.S. Was, in: Proceedings of the 12th Int'l Conference in Environmental Degradation of Materials in Nuclear Systems-Water Reactors, 2005, American Nuclear Society, UT, p. 1387.
[2] G. Gupta, G.S. Was, in: Proceedings of the 12th Int'l Conference in Environmental Degradation of Materials in Nuclear Systems-Water Reactors, 2005, American Nuclear Society, UT, p. 1359.
[3] S.M. Bruemmer, G.S. Was, J. Nucl. Mater. 216 (1994) 348.
[4] R.W. Hertzberg, Deformation and fracture mechanics of engineering materials, John Wiley, Inc., 1976.
[5] T. Lechtenberg, W.M. Garrison, J.M. Hyzak, in: J.W. Davis, D.J. Michel (Eds.), Ferritic alloys for use in nuclear energy technologies, Met. Soc. AIME, Warrendale, PA, 1985, p. 365.
[6] D.S. Gelles, L.E. Thomas, in: J.W. Davis, D.J. Michel (Eds.), Topical conference for steels in nuclear energy technologies, Met. Soc. AIME, Warrendale, PA, 1984, p. 559.
[7] J.J. Kai, R.L. Klueh, J. Nucl. Mater. 230 (1996) 116.
[8] H.M. Kim, J.A. Szpunar, Mater. Sci. Forum 157–162 (1994) 753.
[9] G. Palumbo, P.J. King, P.C. Lichtenberger, K.T. Aust, U. Erb, Mat. Res. Soc. Symp. Proceedings 238 (1992) 311.
[10] E.M. Lehockey, A.M. Brennenstuhl, I. Thompson, Corros. Sci. 46 (2004) 2383.
[11] B. Alexandreanu, PhD Thesis, University of Michigan, 2002.
[12] G. Gupta, G.S. Was, J. ASTM Int. 2 (3) (2005), March.
[13] G. Gupta, G.S. Was, TMS Lett. 2 (3) (2005) 71.
[14] T.R. Allen, L. Tan, Y. Chen, X. Ren, K. Sridharan, G.S. Was, G. Gupta, P. Ampornrat, Presented at Global 2005 Conference, Tsukuba, Japan, October 9–13, 2005, p. 419.
[15] G. Gupta, B. Alexandreanu, G.S. Was, Metall. Mater. Trans., February 2004, 35 A, Research Library, p. 717.
[16] A. Anders (Ed.), Handbook of Plasma Immersion Ion Implantation & Deposition, John Wiley, New York, 2000, p. 553.
[17] G. Gupta, A.N. Ham, Z. Jiao, J.T. Busby, G.S. Was, J. Nucl. Mater. 351 (1–3) (2006) 162.
[18] X. Ren, L. Zheng, K. Sridharan, T.R. Allen, in: D.J. Folkerts (Ed.)., Trans. American Nuclear Society Annual Conference, Materials for Supercritical Water Reactors, San Diego, CA, vol. 92, June 2005, p. 119, ISSN: 003-018X.
[19] A. Alamo, X. Averty, Progress Report UT-SM& C-LAM2, CEA report, NT SRMA 99-2316, April 1999.
[20] C.J. McMohan Jr, in: L.J. Bonis, J.J. Duga, J.J. Gilman (Eds.), Fundamental phenomena in the materials sciences, vol. 4, Plenum, New York, 1967, p. 247.
[21] George E. Dieter, in: Mechanical Metallurgy, 2nd Ed., McGraw-Hill International Book Company, 1981.
[22] H. Hannemann, A. Brode, Atlas Metallographicus, 1933, 1, plates 88 to 90, berlin verlag von gebruder borntraeger.
[23] N.P. Allen, W.P. Rees, B.E. Hopkins, H.R. Tipler, J. Iron Steel Inst. 174 (1953) 108.
[24] S.F. Pugh, in: An introduction to grain boundary fracture in metals, The Institute of Metals, 1 Carlton House Terrace, London SW1Y 5DB, 1991.
[25] Bradley Dodd, Yilong Bai, Ductile Fracture and Ductility with Applications to Metalworking, United States Edition, Academic Press, Orlando, Florida 32887, 1987.
[26] J.M. Vitek, R.L. Klueh, Met. Trans. A 14 A (1983) 1047.
[27] R.L. Klueh, D.R. Harries, High-chromium ferritic and martensitic steels for nuclear applications, ASTM stock number: MONO3.
[28] R.H. Jones, Stress-Corrosion Cracking – Materials Performance and Evaluation, ASM International Materials Park, Ohio 44073-0002, 1992.
[29] L. Schafer, J. Nucl. Mater. 258–263 (1998) 1336.

[30] L.K. Singhal, J.W. Martin, Trans. Metall. Soc. AIME 242 (1968) 814.
[31] Y.S. Lim, J.S. Kim, H.P. Kim, H.D. Cho, J. Nucl. Mater. 335 (2004) 108.
[32] G. Eggeler, A. Dronhofer, J. Pesicka, Steel research 76, 2005, Issue 9/2005, 656.
[33] Steven Van Dyck, Presented at 2001 Eurocorr Conference in Riva del Gardia, Italy.
[34] G.S. Was, S. Teysseyre, Z. Jiao, Corrosion, in press.
[35] R.L. Klueh, J.M. Vitek, J. Nucl. Mater. 137 (1985) 44.
[36] P.J. Maziasz, R.L. Klueh, J.M. Vitek, J. Nucl. Mater. 141–143 (1986) 929.
[37] Y. Chen, K. Sidharan, T.R. Allen, Corros. Sci., in press.